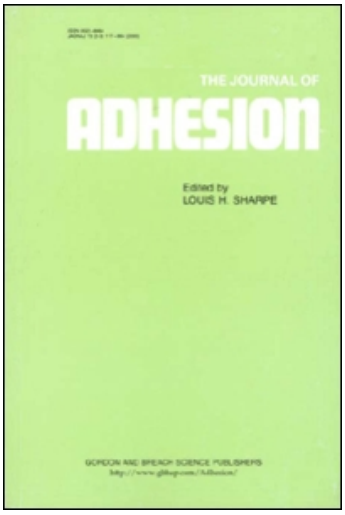

The Journal of Adhesion
Publication details, including instructions for authors and subscription information:
http://www.informaworld.com/smpp/title~content=t713453635

Modelling the Environmental Degradation of the Interface in Adhesively Bonded Joints using a Cohesive Zone Approach

C. D. M. Liljedahl[a]; A. D. Crocombe[a]; M. A. Wahab[a]; I. A. Ashcroft[b]
[a] School of Engineering, University of Surrey, Guildford, United Kingdom [b] Wolfson School of Mechanical and Manufacturing Engineering, Loughborough University, Loughborough, United Kingdom

To cite this Article Liljedahl, C. D. M. , Crocombe, A. D. , Wahab, M. A. and Ashcroft, I. A.(2006) 'Modelling the Environmental Degradation of the Interface in Adhesively Bonded Joints using a Cohesive Zone Approach', The Journal of Adhesion, 82: 11, 1061 — 1089
To link to this Article: DOI: 10.1080/00218460600948495
URL: http://dx.doi.org/10.1080/00218460600948495

The Journal of Adhesion, 82:1061–1089, 2006

ISSN: 0021-8464 print/1545-5823 online
DOI: 10.1080/00218460600948495

Taylor & Francis
Taylor & Francis Group

Modelling the Environmental Degradation of the Interface in Adhesively Bonded Joints using a Cohesive Zone Approach

C. D. M. Liljedahl
A. D. Crocombe
M. A. Wahab
School of Engineering, University of Surrey, Guildford, United Kingdom

I. A. Ashcroft
Wolfson School of Mechanical and Manufacturing Engineering, Loughborough University, Loughborough, United Kingdom

The use of a cohesive zone model (CZM) to predict the long-term durability of adhesively bonded structures exposed to humid environments has been investigated. The joints were exposed to high relative humidity (RH) environments and immersion in both tap and deionised water for up to a year before quasi-static testing to failure. Both stressed and unstressed conditions during aging were considered. The degradation was faster for the stressed joints and for those joints immersed in the more corrosive environments. Two mechanisms were suggested to explain this behaviour: cathodic delamination and stress-enhanced degradation. In the model, the cohesive zone parameters determine the residual strength of the joints. The degradation of these parameters was, in the first instance, related directly to the moisture concentration. The model was then extended to include degradation due to stress and more corrosive environments. Good correlation between the numerical modelling and the experimental results was obtained.

Keywords: Cohesive zone model; Durability modelling; Finite element; Progressive failure; Residual strength

1. INTRODUCTION

Adhesives are increasingly being used in the aerospace and automotive industries instead of conventional bonding. Their main advantages are

Received 7 March 2006; in final form 12 July 2006.
Address correspondence to A. D. Crocombe, School of Engineering, University of Surrey, Guildford, GU2 7XH, UK. E-mail: a.crocombe@surrey.ac.uk

their ability to bond dissimilar materials and the large stress-bearing area, which results in lower stress concentrations in comparison with rivets and bolts. The major disadvantage is the reliability of the bond strength in humid environments. Hence, it is of great importance to be able to predict the long-term durability to better understand the degradation process and, at the same time, reduce the amount of expensive and time-consuming durability testing in the development and certifying stages of product development.

To be able to assess the integrity of a bonded structure, the moisture profile throughout the joint has to be determined. Diffusion in adhesives has been modelled extensively and accurately by Fick's second law [1–4]. Neumann and Maron [5] have investigated the stress dependence of absorption in polymeric composite materials and found a slight increase in the uptake rate for stressed samples. Petropoulus and Sanopoulou [6] have determined stress-dependent diffusion experimentally by means of colored tracer and bi-refringence profile measurements. A sharp diffusion front between the swollen and unpenetrated polymer was seen (Case II kinetics). Roy *et al.* [7] have measured uptake in epoxy adhesives bonded onto aluminium sheets. The assembly was bent to induce a strain in the adhesive during the uptake. An increase in diffusivity of 32% was found at 10% strain for aging at 50°C and 95% relative humidity (RH).

In the absence of water, the work of adhesion is positive, but in the presence of water, the relation gives a negative value, and hence, the interface becomes thermodynamically unstable [8]. However, the thermodynamic approach describes a joint at equilibrium but not how long it takes to achieve this state. The fracture energy was seen to decrease with an increase in the RH of the aging environment [9]. The degradation can also be explained by considering the interfacial chemistry; the strength of bonds that water forms with an inorganic oxide is substantially greater than the interactions between an oxide and a polymer [10].

Yet other possible mechanisms of degradation of the interface are cathodic delamination or electrochemical-corrosion [11]. Kinloch *et al.* [12] have suggested that the inferior strength of a tapered double cantilever beam (TDCB) joint when immersed in water compared with 100% RH might have been due to such a corrosion process. The role of ion diffusion in the cathodic-delamination process for coated steel has been determined by Deflorian and Rossi [13]. The rate of delamination was seen to be a function of the salt concentration in the solution. In distilled water, the delamination was almost unmeasurable. However, the induction time was determined by the diffusion of water through the coating. The same characteristic has been found by Sargent [14]. Specimens immersed in tap water failed

early on in the test, and specimens immersed in distilled water did not show any significant reduction in strength even after 7 years.

Covalent bonds might exist across the interface in a joint [15]. Any chemical reaction involving the destruction of these bonds would be accelerated under the application of stress. Lam *et al.* [16] derived a relation for debonding through hydration using chemical kinetics and thermodynamics. Comparison between the model and experimental crack-length data gave good agreement, and the authors concluded that this indicated that the bond degradation was governed by time-dependent, stress-assisted hydration rather than by the water alone.

Peak strains (or stresses) have been used extensively to predict the joint strength of adhesively bonded joints [17–20]. However, it is, difficult to use this method because of the bimaterial singularities inherent in a bonded joint. This imposes a problem when analysing the stresses in a joint. Crocombe [21] has suggested global yielding as a failure criterion for bonded joints. The author emphasised that this can give a good prediction of the failure load in certain cases. Failure usually initiates at a small crack or flaw, and hence, fracture mechanics is a versatile method for evaluating the strength of joints or the resistance to crack initiation and crack growth. Fracture mechanics have been used to predict joint strengths by many researchers [22,23]. However, this approach is only valid under small-scale yielding and is not appropriate when there is gross plastic deformation before failure. Another approach to model the strength and progressive damage is through a cohesive zone model (CZM). When using a CZM, the interface strength is governed by a traction separation law. A CZM has been used to simulate and predict the behaviour of a wide range of bonded joints successfully in dry conditions [24–27]. Crocombe *et al.* [28] and Liljedahl *et al.* [29] have used a CZM to predict the long-term durability of adhesive bonded joints successfully. However, adhesive plasticity was not included.

In this study, the durability of adhesively bonded joints exposed to humid environments was investigated. The effect of corrosive environments and stress during aging are discussed, and an approach to include this in the CZM is described.

2. MATERIAL PROPERTIES AND EXPERIMENTAL RESULTS

During this study, a mixed mode flexure (MMF) adhesive joint fracture specimen, a notched coating adhesive (NCA) specimen, a single-lap joint (SLJ), and an L-joint were tested. A heat-cured film adhesive (FM73 from Cytec Engineered Materials, Tempe, AZ, USA) was used to bond all specimens.

The environments in which the joints were aged before testing at room temperature were 80%RH/70°C, 96%RH/50°C, and immersion in water (tap and deionised) at 50°C.

2.1. Adhesive

The adhesive used in this investigation was the heat-curing, toughened epoxy adhesive FM73 (Cytec). The FM73 film was yellowish with a nominal thickness of 0.18 mm. Dumbell specimens were manufactured to determine the material properties of the bulk adhesive. To manufacture a cured adhesive sheet of 0.5 mm in thickness, four layers were stacked together. The adhesive compound was degassed in a vacuum oven at 80–90°C for approximately 10 min before cure to prevent voiding in the samples. The best results were obtained by cycling this technique a number of times. A release film, a glass plate, and a weight were then placed on top on the adhesive stack, and the compound was cured at 120°C for 1 h as suggested by the manufacturer. Spacers were used to control the resulting sheet thickness. After cure, dumbbell specimens of overall length of 65 mm, gauge length of 30 mm, and width of 5 mm were cut with a computer numerical control (CNC) machine.

The moisture uptake in the adhesive in the various environments was determined with gravimetric experiments, carried out on the bulk adhesive dumbell specimens. The results are given in Table 1. The uptake rate was strongly dependent on the temperature but essentially unaffected by the moisture saturation level. The saturation level increased, as expected, with the RH for all bulk specimens.

The coefficient of thermal expansion (CTE) was determined by means of a bimaterial beam, consisting of a thick layer of adhesive (1.1 mm) cast on a thin high-strength steel strip (0.2 mm). The residual stresses induced following cooling to room temperature caused the strip to bend. The deflection of the curved strip as a function of the temperature was measured with an LVDT (linear variable differential transducer). From these data, the coefficient of thermal coefficient of

TABLE 1 Moisture-Uptake Parameters for the Adhesive FM73

Adhesive	Relative humidity (%)	Temperature (°C)	Saturation content (%)	Diffusion coefficent (10^{-14} m^2/s)
FM73	Immersion	50	1.2	52.2
FM73	95.8	50	2.2	50.2
FM73	79.5	70	2.5	790.0

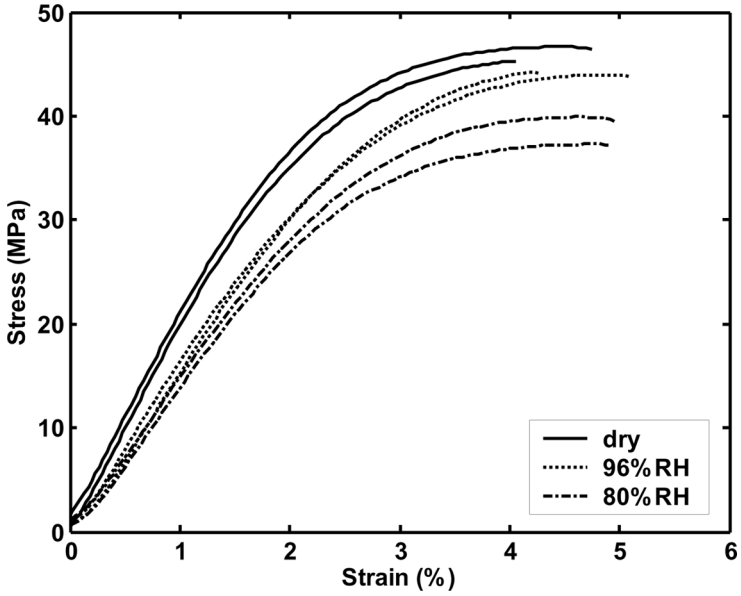

FIGURE 1 Bulk stress–strain curves at various moisture levels.

the adhesive can be determined [30]. The CTE was found to be $7.7 \times 10^{-5} K^{-1}$.

The swelling of the adhesive was determined by measuring the expansion of the dumbell specimen with a shadow graph (Mitutoyo Profile Projector PJ 300, Kawasaka, Japan). The samples were removed periodically from the aging environment and weighed, and the length of the specimens was measured. The swelling was found to be linear with the moisture content and to be 0.0021 ($\%^{-1}$). This is a trend that has been observed by other researchers with different adhesive systems [31].

The mechanical properties were determined by testing dumbell specimens in tension in displacement control mode at 1 mm/min at room temperature after saturation in the aging environments (50°C/96% RH and 70°C/80% RH). Typical results from these are given in Fig. 1. The results are summarised in Table 2. The elastic modulus and the ultimate tensile strength both decreased as the polymer network became plasticised by moisture. After saturation in the 96% RH environment, the modulus decreased by 25% and the ultimate strength by 15%. A value of 0.4 was used for the Poisson's ratio.

The viscoplastic properties of the adhesive were determined by carrying out creep tests at the aging temperature at three stress levels,

TABLE 2 Mechanical Properties for the Adhesive at Various Moisture Concentrations at 20°C

Adhesive	Environment	Moisture content (%)	E (MPa)	σ_{uts} (MPa)
FM73	Dry	0.0	2000	45
FM73	80%RH/70°C	1.1	1700	42
FM73	96%RH/50°C	2.2	1500	38

after saturation in the aging environments. The same configuration of dumbell film specimen was used as in the tensile test. After aging, the specimens were wrapped in soaked cotton wool and then in thin plastic film to retain the moisture. The wrapped specimen was then placed in a pre-heated temperature cabinet on the test machine, and an extensometer were used to measure the strain. The extensometer data was stored on a datalogger regularly throughout the test. The specimen was loaded in tension at 1 mm/min until the creep load was reached. The load was then held constant. The results can be seen in Fig. 2. The resistance to creep was seen to decrease in the presence of moisture, but even after saturation in water, it remained very resistant compared with another adhesive tested by the authors [29]. The

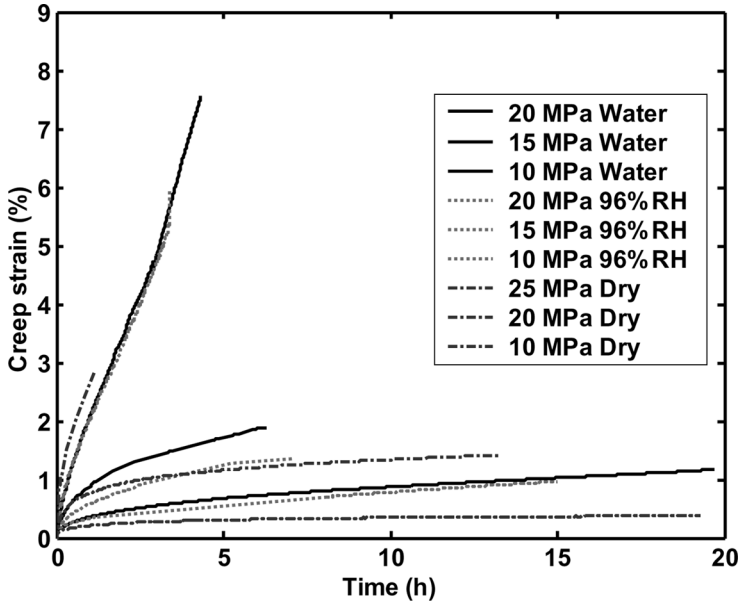

FIGURE 2 Creep data for various moisture concentrations.

TABLE 3 Creep Parameters at 50°C (Force (N), Length (mm), Time (s), Stress (MPa))

Condition	A	n	M
Dry	6.5458×10^{-11}	4.75	–0.6
96%RH	1.3493×10^{-10}	4.75	–0.5
Immersion	1.5848×10^{-10}	4.75	–0.5

experimental data were fitted to a power law [Eq. (1)] to be able to use the data in the modelling:

$$\dot{\varepsilon}_{creep} = Aq^n t^m \tag{1}$$

where a dot represents differentiation with respect to time, q is equivalent stress, t is the time, and A, n, and m are constants. The best-fit creep parameters are given in Table 3.

2.2. Substrate

The elastic modulus of the aluminium (7075 T6) was determined with a tensile test (BS EN 1386:1997) and was found to be 68400 MPa. A Poisson's ratio of 0.33 was used for the aluminium. The CTE used for the aluminium alloy was $2.36 \times 10^{-5}\,K^{-1}$.

Before bonding, the aluminium alloy substrates were pretreated in a chromic acid etch solution (CAE) according to DEF STAN 03-2/ Issue 3. All joints were cured for 1 h at 120°C.

2.3. Fracture Toughness

The fracture toughness, after saturation in the aging environments, was determined using MMF and NCA specimens. Both specimens were open faced during the aging process. This gave a shorter aging time and a uniform moisture distribution along the interface.

An NCA specimen is a coated substrate. Following aging, the coating is cut (notched) across the centre of the specimen, as shown in Fig. 3. The specimen was then loaded in tension, and the strain at

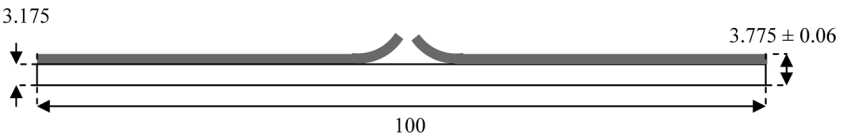

FIGURE 3 Dimensions of the NCA specimen (width 12.7) (all dimensions in mm).

which the coating debonded from the substrate gave a measure of the interfacial strength. The length, width, and thickness of the 7075 T6 aluminium substrate used to manufacture the NCA specimen were 100 mm, 12.7 mm, and 3.175 mm, respectively. The thickness of the coating was 0.6 mm. A poly(tetrafluoro ethylene) (PTFE) film was used to form the precrack. After curing, the specimen was saturated in deionised water at 50°C. The specimen was then removed from the aging environment and loaded in tension at 1 mm/min, and the strain when the adhesive layer debonded was recorded using an *in situ* video microscope. Further strain-induced crack-length data could not be obtained because of the speed of the crack growth following initial debonding. The experimental results are shown in Fig. 4. It proved more difficult to use the NCA test at 95% RH, 80% RH, and unaged conditions because the coating tended to crack before debonding occurred. Thus, the MMF configuration was used for these aging conditions.

The MMF specimens are shown in Fig. 5. Specimens to be tested unaged were assembled and cured in one step. A PTFE film was used to form the precrack. For the aged specimens, the coated substrate was exposed to the environment and left to saturate as for the NCA specimen. After exposure, the specimen was removed from the

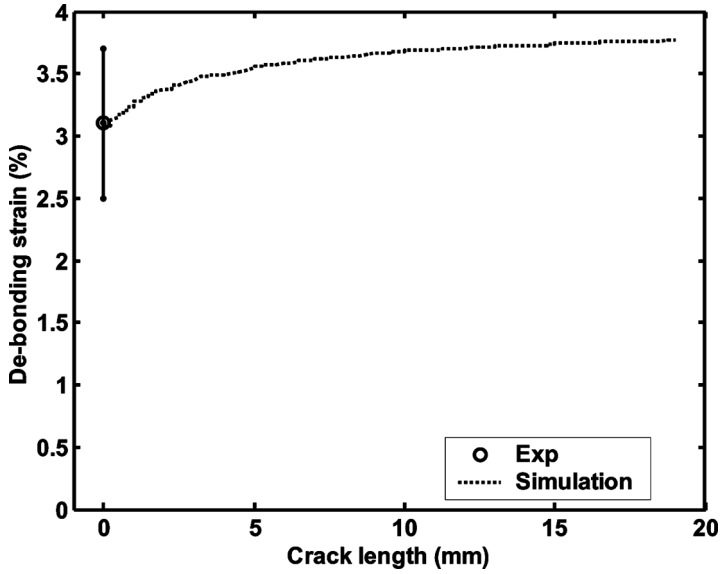

FIGURE 4 Experimental results and simulation of the NCA specimen aged by immersion in deionised water.

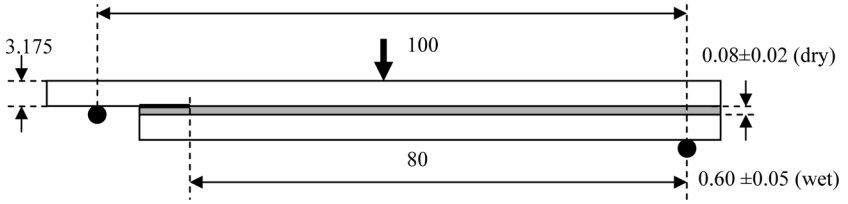

FIGURE 5 Dimensions of the MMF specimen (width 12.7) (all dimensions in mm).

environment, abraded, and cleaned with acetone. A secondary bond adhesive (Hysol EA9321, Henkel, Düssldorf, Germany) was then applied, and the assembly was allowed to cure in the aging environments for 6 days. After curing, the specimen was removed from the environment and the excess adhesive on the sides was removed to facilitate the monitoring of the crack growth. The specimen was then tested at room temperature. The MMF specimen was used to obtain the fracture toughness for the adhesive system in the unaged condition and after saturation in the 80% RH and 96% RH environments. The dimensions for the MMF are given in Fig. 5.

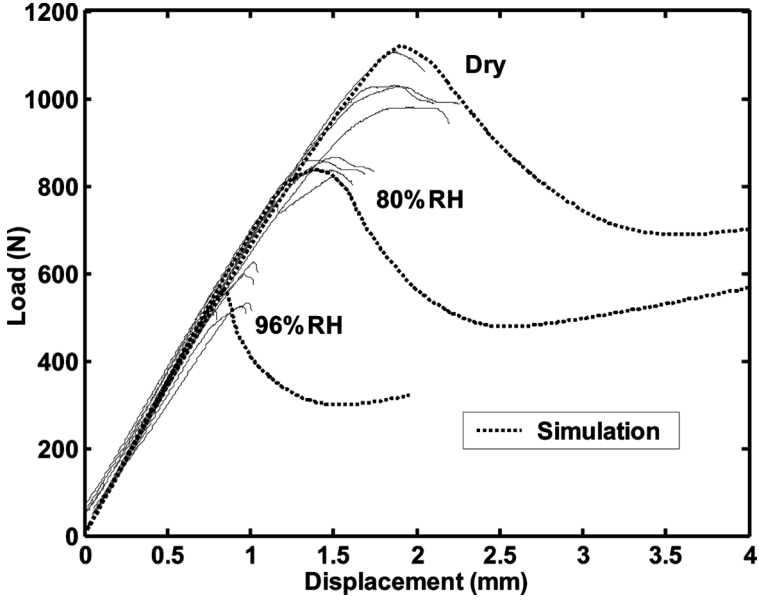

FIGURE 6 Experimental results and modelling for the MMF specimen (load-displacement).

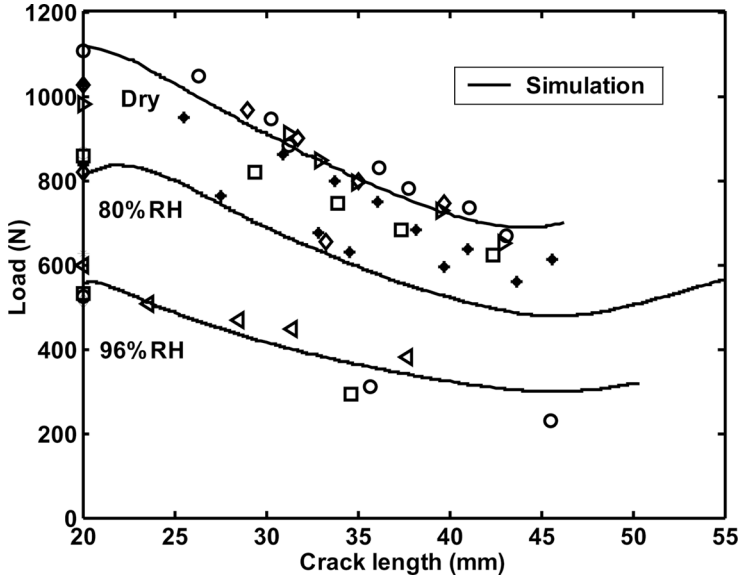

FIGURE 7 Experimental results and modelling for the MMF specimen (load crack length).

The specimen was supported by rollers and loaded in displacement control at 0.05 mm/min. Results are shown in Figs. 6 and 7. The failure load dropped significantly in the presence of moisture. For both the dry and for the MMF saturated at 80% RH, the load-displacement curve showed a smooth peak around the maximum load, whereas, the specimen saturated in the 96% RH exhibited a more abrupt decrease in load after the peak load was reached. This was due to the change in failure locus after aging at 96% RH. The interface was the weakest link of the joint after aging in 96% RH, whereas the failure was cohesive (near the interface) for the other two environments. On initial detection of crack growth, the test machine was stopped and the crack length measured using an *in situ* video microscope. The specimen was then loaded again and stopped upon subsequent crack growth, and the crack length was remeasured. This was repeated until the crack had grown to midspan. MMF tests were not undertaken for immersion in water as it proved difficult to produce a secondary bond in these conditions.

2.4. Joint Tests

The joints discussed here are a single-lap joint (SLJ) and an L-joint. Before testing, the joints were immersed in water for up to a year.

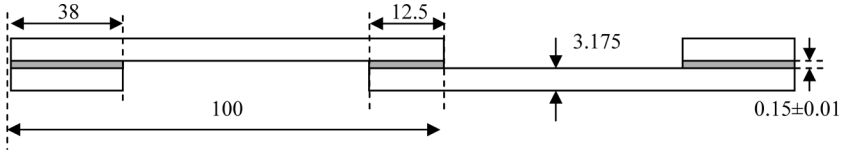

FIGURE 8 Dimensions of the SLJ (all dimensions in mm).

The joints were tested at 1 mm/min, and the dimensions are given in Figs. 8 and 9. The L-joint was loaded in a three-point pulloff configuration; *i.e.*, the skin was supported by rollers, and a displacement was applied on the stringer (vertical leg of the angle). The experimental results are plotted in Figs. 10 and 11. For both the stressed and the unstressed SLJ, the load initially dropped rapidly and then levelled off, decreasing at a lower rate. The reduction before levelling off was, however, more severe for the stressed SLJ. The strength for the stressed SLJ apparently increased for the specimens aged for the longest time. This increase in strength is not yet fully understood.

The failure mode for the dry joint was mainly cohesive. For the wet joint, the amount of interfacial failure increased with aging time. The failure surfaces of the SLJ after immersion for 26 weeks are shown in Fig. 12. The failure surface of the L-joint after 30 weeks of immersion can be seen in Fig. 13. From the figures, it can be seen that the interfacial damage was apparently more severe for the stressed SLJ and the L-joint than for the unstressed SLJ.

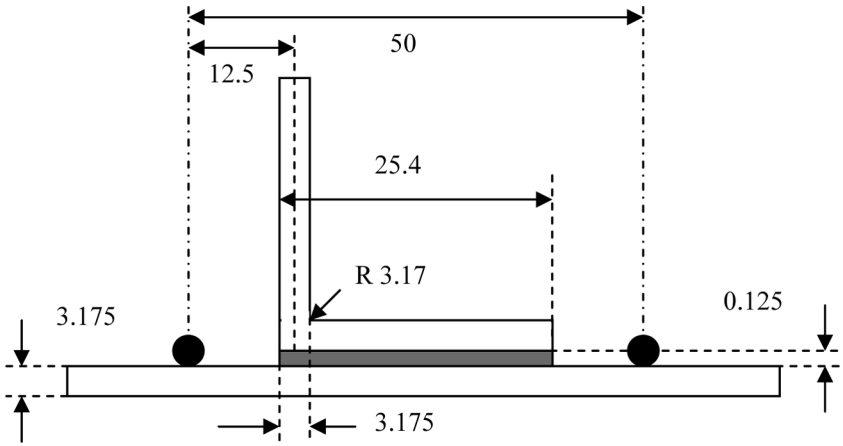

FIGURE 9 Dimensions of the L-joint (width 25, R 0.76 on the flange where not given) (all dimensions in mm).

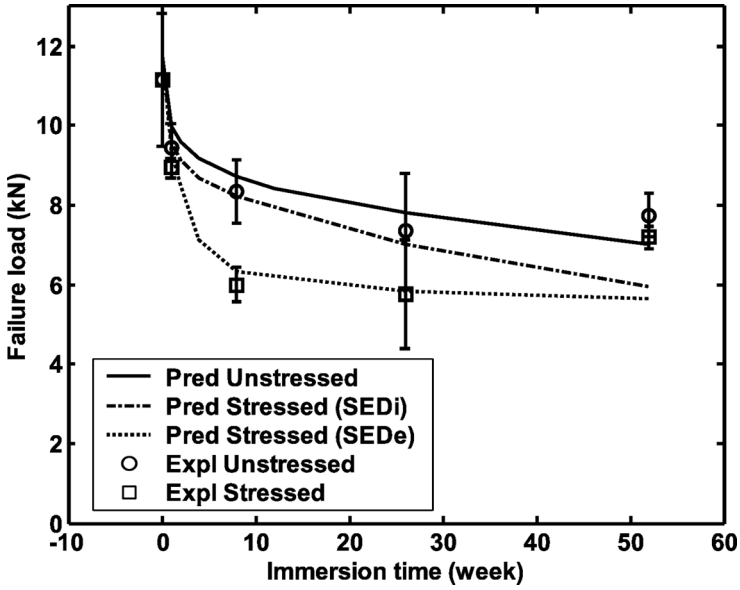

FIGURE 10 Experimental results and predictions for the SLJ (unloaded and loaded at 800 N).

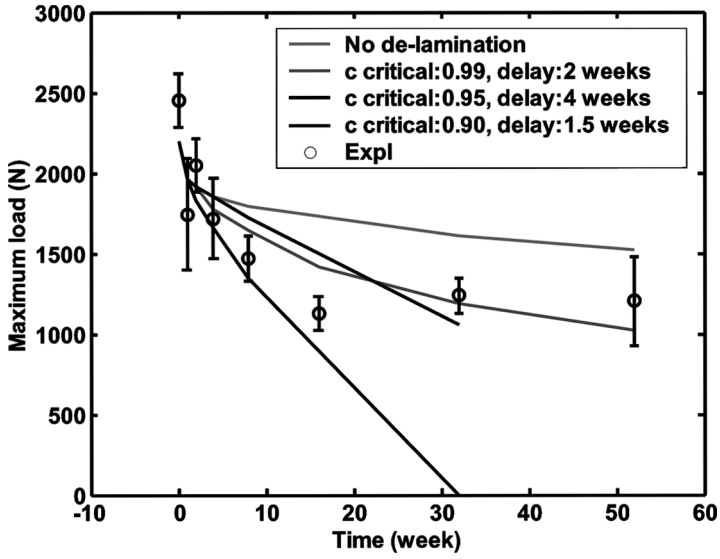

FIGURE 11 Experimental results and predictions for the L-joint.

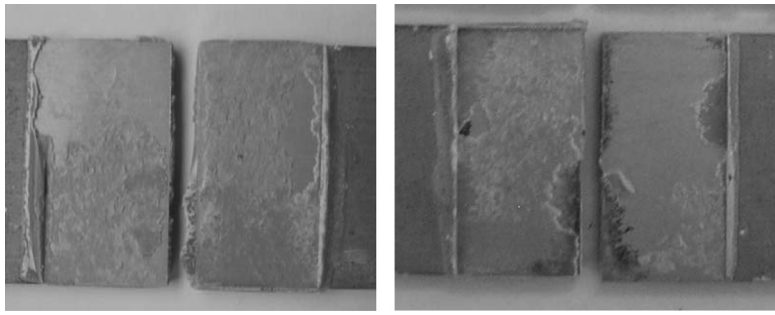

(a) (b)

FIGURE 12 Failure surfaces for the SLJ after 26 weeks for the a) SLJ (unstressed) and b) SLJ stressed.

3. MODELLING

The failure response of the joint was simulated using a CZM. A two-parameter CZM was used where separations in modes I, II, and III were accounted for. However, the fracture energy (which determines material failure, Fig. 14) in all modes was the same. The CZM parameters were the energy (Γ_0) and the tripping traction (σ_u). The stiffness before unloading was set high to avoid any significant compliance of the CZM element before the onset of damage (Fig. 14). Plasticity and creep have been incorporated in the adhesive continuum elements as outlined in the next few paragraphs. The commercial FE (finite element)

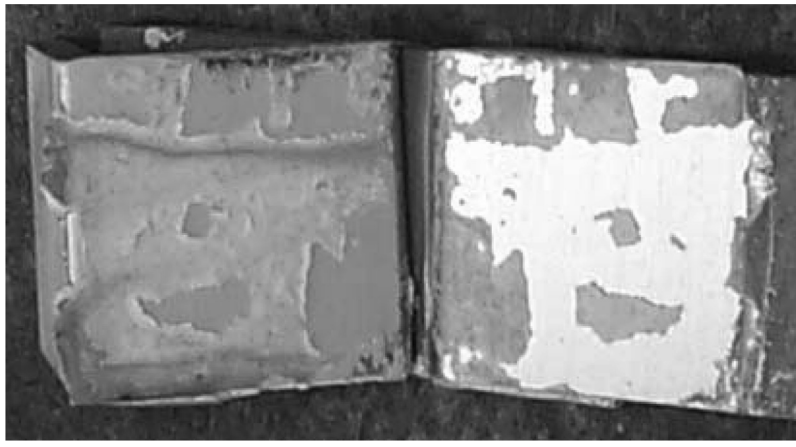

FIGURE 13 Failure surfaces for the L-joint after 30 weeks of immersion.

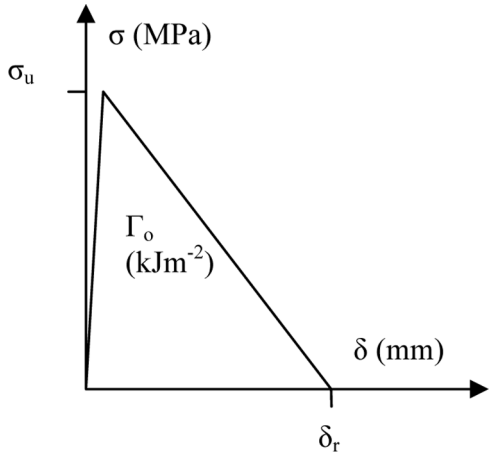

FIGURE 14 Shape of the CZM used throughout the study.

package, ABAQUS (Hibitt, Karlsson & Sorensen, Inc., Pawtucket, RI, USA) was used for all the numerical modelling work. Nonlinear springs (ABAQUS 6.5: 18.1.1) were used to specify the traction–separation law at the interface in the two-dimensional (2D) modeling. In the three-dimensional (3D) model, the traction–separation law was modelled with ABAQUS CZM elements (ABAQUS 6.5: 18.5.1) as these became available only after the 2D modelling work had been completed. The responses of the two different elements were shown to be equivalent.

CZM is CPU intensive, and therefore, it was convenient to model the joints in 2D if appropriate. Extensive diffusion and stress analysis without CZM elements were, thus, carried out to determine if 2D models could be used. First, assessment of the diffusion in 2D and 3D modelling was undertaken. Then stress analysis (linear material properties but nonlinear geometry) was carried out to determine for which joints a 2D model could be used. Additionally, the residual stresses due the mismatch of thermal expansion and swelling in the joints were compared with the mechanical stresses at the failure load to determine if these had to be included in the CZM. For the NCA and the MMF specimens, only saturated conditions were considered, and the diffusion did not need to be modelled explicitly. It was found that the diffusion in the SLJ could be modelled accurately in 2D as the width was twice as long as the overlap and, thus, diffusion from the sides was less significant. However, the L-joint had to be modelled in 3D as the overlap was square.

The stresses in the NCA specimen were found to be accurately modelled assuming plane stress conditions. This was because the coating was thick and constrained only by a substrate on one side. The dry MMF specimen was best represented with plane stress in the substrate and plane strain in the adhesive. The wet MMF specimen, having a thicker adhesive layer, was best represented with plane stress in both the adhesive and the substrate. The substrate was not constrained in the width direction, and this was why the plane-stress assumption was a good representation of the stress state. Plane strain did represent the adhesive stress state better for the specimen with a thin adhesive layer as it was heavily constrained by the substrate. However, the thick adhesive layer allowed for some movement in the width direction, and therefore, plane stress was seen to accurately represent the adhesive stress state in these joints. The SLJ was modelled accurately assuming plane-strain conditions as the adhesive was constrained by the substrates and the adhesive layer was thin. Neither thermal nor swelling residual strains were significant and did not have to be included. In other work, not reported here [32], joints had mixed substrates and the residual stresses were then more significant.

Analyses were also undertaken using von Mises and a linear Drucker–Prager plasticity model (ABAQUS 6.5: 11.3.1). When using von Mises plasticity and the experimentally determined stress-strain curve (Fig. 1), global collapse occurred for the SLJ at a load lower than the experimental failure load. This clearly indicated the need for the more advanced pressure-dependent Drucker–Prager yield model. Using a friction angle (the angle between the horizontal axis and the initial yield curve in the equivalent stress–hydrostatic pressure space) of 32.5° in the Drucker–Prager model resulted in a global collapse load higher than the experimental failure load and was similar to the friction angle used by Wang and Chalkley [33]. Adhesive plasticity had to be included in the modelling because the fracture energy initially increased with crack length for the MMF specimen. This R-curve behaviour could only be simulated when using adhesive plasticity. This aspect has been discussed in much greater detail elsewhere [34] for the unaged joints.

The CZM in the following sections was, undertaken in 2D where appropriate, as discussed previously. First, the CZM parameters were determined for various moisture concentrations using the MMF and NCA specimens. These parameters were then used to predict the response of the SLJ. Finally, the response of the L-joint was predicted. The adhesive continuum was modelled using a linear Drucker–Prager model, as explained previously, with a friction angle of 32.5° and

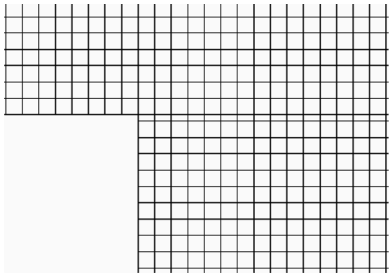

FIGURE 15 Mesh used for the MMF specimen.

moisture-dependent hardening as determined experimentally (Fig. 1). Creep was included when modelling the aging of the stressed SLJ, using the parameters in Table 3.

Initial CZM modelling of the MMF specimen was undertaken to assess mesh effects. Four noded plane-strain elements were used, and the finer mesh can be seen in Fig. 15.

The effect of the predicted failure load at two different energy levels and for various tripping tractions can be seen in Fig. 16. The response was mesh independent if the CZM properties were chosen so that they resulted in a response below the region where the process zone length (PZL) became discontinuous. The CZM properties used throughout this study operated in this mesh-independent region.

3.1. Determination of Time Independent CZM Parameters for the Aging Environments

The CZM parameters were determined from the MMF specimen for unaged conditions and for saturation at 80% RH and at 96% RH. The mesh used for the MMF model with the thicker adhesive layer specimen is shown in Fig. 15. Four noded elements were used, and the smallest element along the crack path was 0.25 mm. The upper interface strength was modelled with CZM elements as the precrack was at that interface.

The tripping traction was determined by the onset of nonlinearity in the load-displacement response (Fig. 6). The fracture energy (Γ_0) was then determined by correlating the simulated load–crack length characteristics with the experimental results (Fig. 7). This gave a unique set of CZM parameters for each of the aging environments. The simulations using the calibrated parameters are shown in Figs. 6 and 7. The excellent match between experiment and simulation is clear.

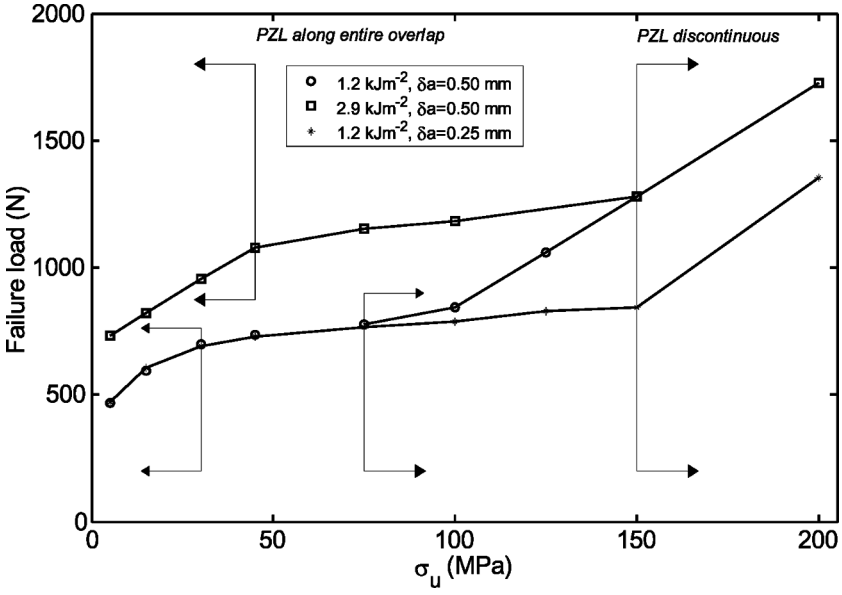

FIGURE 16 Effect of the CZM parameters (elastic adhesive continuum).

The CZM parameters for saturation by immersion in water were determined from the NCA test. The debond strain obtained from the model was correlated with the recorded initial experimental debond strain. The results can be seen in Fig. 4.

The moisture-dependent fracture energy and tripping traction parameters determined from the MMF and NCA calibrations are shown in Fig. 17. The fracture energy was seen to decrease rapidly initially and then flatten out, whereas the opposite occured for the tripping traction.

3.2. Prediction of the Aluminium Single-Lap Joint

The determined CZM parameters were used in this section to predict the durability of the SLJ. The prediction was undertaken in two steps. First, the moisture profile throughout the joint was predicted in a diffusion analysis. Then, the predicted moisture profile was read in as a predefined field in the subsequent CZM of the SLJ because both the adhesive continuum and CZM parameters were a function of the moisture concentration (Figs. 1 and 17). The mesh used for the SLJ throughout this section is shown in Fig. 18. The fillet was modelled to get as accurate a correlation between the model geometry and the experimental test specimen as possible.

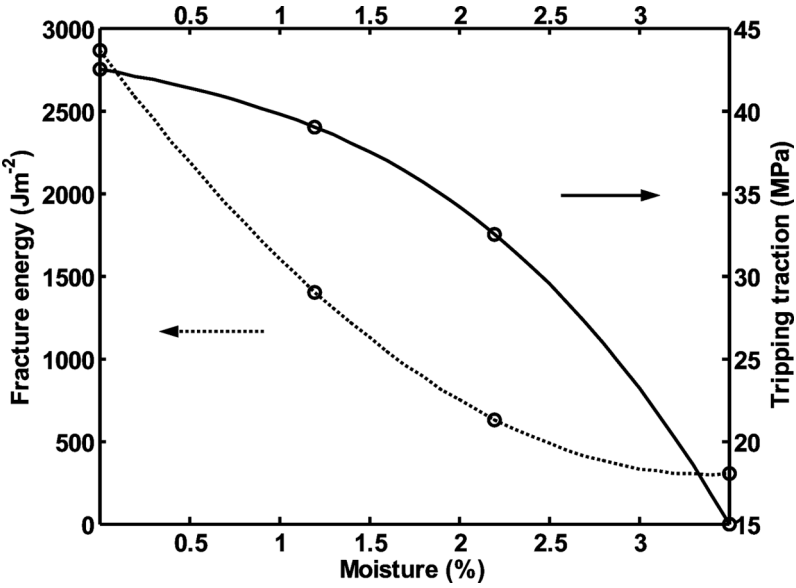

FIGURE 17 Determined moisture-dependent tripping traction and fracture energy.

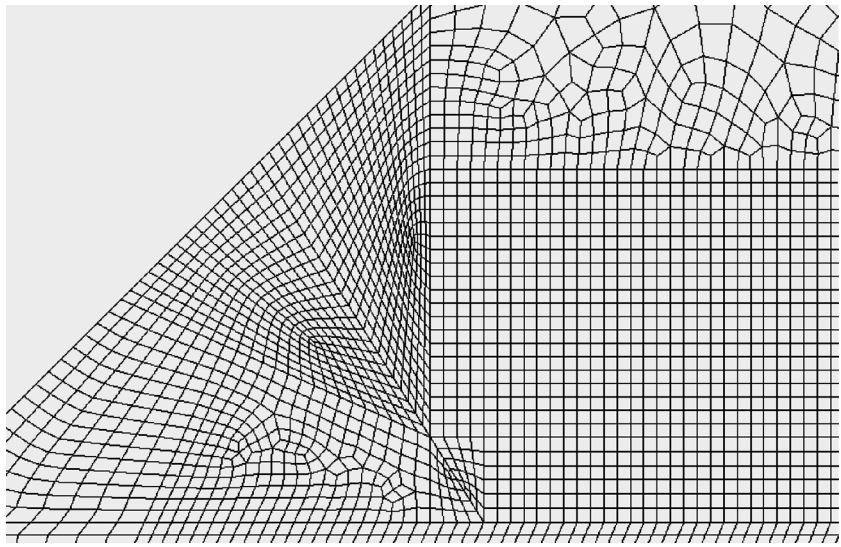

FIGURE 18 Mesh used for the SLJ.

In the first section, the modelling of the unstressed SLJ is discussed, and in the second section, approaches to model stress-dependent effects are developed.

3.2.1. Unstressed SLJ

The prediction of the unstressed SLJ was undertaken as described previously. First, diffusion analysis for the different aging times was carried out. The predicted field was then read in as a predefined field in the progressive damage modelling to model the response and the failure load of the SLJ. The results are given in Fig. 9. The predicted response is seen to correlate well with the experimental results.

The predicted damage initiation and crack growth in a dry and a wet SLJ can be seen in Fig. 19. The dashed and the solid lines represent damage initiation and material rupture, respectively. From the graph it can be seen where the damage initiated on the overlap and the characteristics of the subsequent crack propagation through the joint. For both the dry and the wet joints, the damage initiated at the bimaterial interface corner (Fig. 20). The crack then propagated through the fillet in the dry joint. After the fillet failed, the joint failed

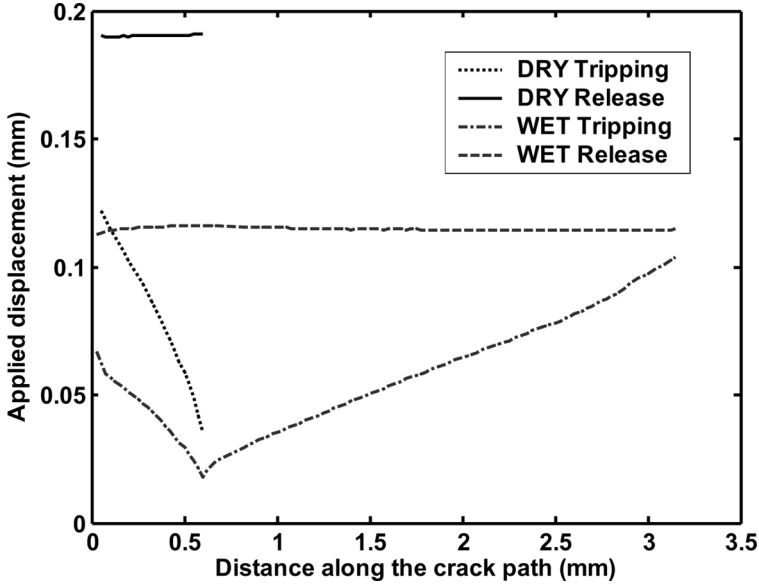

FIGURE 19 Failure paths through dry and aged (365 days in water) aluminium SLJ.

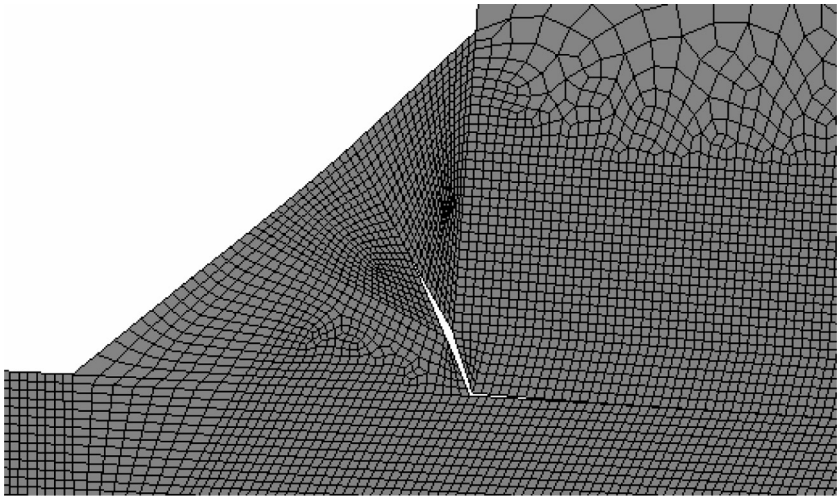

FIGURE 20 Damage in the wet SLJ (8× magnification of the displacements).

by limit state collapse because the tripping tractions could not be achieved. This was due to the large plastic zone around the cracked fillet as the load now was carried by the part of the overlap not yet yielded. However, the failure load was, governed by the initial failure of the CZM elements in the fillet region. For the wet joint, damage initiated over the whole overlap before failure occurred catastrophically by rapid crack propagation through the entire overlap.

3.2.2. Stressed SLJ

The strength of the stressed lap joints during aging was seen to degrade more than the unstressed ones (Fig. 10). The mechanisms considered for this apparent stress-induced effect were stress enhanced degradation and stress-enhanced diffusion. When modelling the stress-enhanced degradation mechanisms, creep was included in the modelling by defining the viscoplastic response using a power law [Eq. (1)]. The parameters derived and given in Table 2 were used and were set to be a function of the current moisture concentration at the material points. However, the creep strain was small (less than the elastic strain) even after exposure for a year at the aging load (800 N). This indicates that the severe degradation was not due to creep failure.

Stress-enhanced diffusion. The ingress of water may be enhanced in the presence of stress and can be related to the change in free

volume by a Doolittle [35] equation [36]:

$$\ln\left(\frac{D_\sigma}{D_0}\right) = \alpha\left(\frac{1}{\vartheta_{f0}} - \frac{1}{\vartheta_{f\sigma}}\right),$$

$$\vartheta_{f\sigma} = \vartheta_{f0} + \left(\frac{\Delta V}{V_0}\right),$$

$$\vartheta_{f0} = M_\infty \frac{\rho_M}{\rho_W},$$

where ϑ_{f0} is the free volume fraction in the unloaded condition, ρ_W and ρ_M are the density of water and matrix, respectively, and α is a constant of proportionality. Both stressed and unstressed volumes relate to the test temperature (50°C), which was the same for both the unloaded and loaded tests.

Neumann and Marom [36] have determined the value of α by fitting the equation to uptake data for an epoxy aged at 52°C under various stress levels. The value of α found was 0.033. Fahmy and Hurt [37] used a value 0.31 to predict the diffusion in stressed epoxy samples. However, this was, determined assuming the polymer to be above the glass transition temperature, and hence, the dependence on stress was overestimated.

The change in free volume is equal to the volumetric strain. Hence, when modelling stress- or strain-dependent diffusion, the diffusion coefficient can be set to be dependent on the volumetric strain:

$$\frac{\Delta V}{V_0} = \varepsilon_x + \varepsilon_y + \varepsilon_z.$$

The stress-dependent diffusion was simulated by defining a solution-dependent field variable as the volumetric strain, using a USFLD FORTRAN subroutine (ABAQUS 6.5: 25.2.39) in a coupled stress-diffusion analysis (ABAQUS 6.5: 6.5.4). A stress dependence based on the volumetric strain corresponding to the higher value of α was used. (This gave an increase of 50% in the diffusion coefficient at 25 MPa uniaxial tension.) The mesh used is showed in Fig. 17. The results for the stress-enhanced diffusion (SEDi) can be seen in Fig. 10. The strength does not reduce sufficiently even though the stress-dependent diffusion was overestimated.

Stress-enhanced degradation (SEDe). The other mechanism considered was stress-enhanced degradation. The approach used to model this is described next.

A chemical reaction can often be described by a first-order equation. The degradation due to stress was, thus, included in the following manner:

$$-\frac{dS}{dt} = A \times c \times \sigma \times S,$$

where A is a constant, c is the moisture concentration, S is the (stress-degraded) retained strength ratio (varying from 1 to 0), and σ is the equivalent stress. No stress-dependent degradation was assumed to occur if the stress was below a threshold stress (σ_t), following an approach often used in fatigue testing.

The rate of degradation was assumed to be much faster than the moisture ingress and therefore could be related directly to the moisture concentration. The equivalent moisture concentration (c_{eq}), which takes both moisture and stress dependence into account, was thus postulated as:

$$c_{eq} = c + (1 - S) \times (c_{sat} - c),$$

where c is the moisture concentration and c_{sat} is the saturation content in water. When there are no stresses in the joint, $S = 1$ and $c_{eq} = c$. This is consistent with the approach outlined for unstressed SLJ in Section 3.2.1. When stresses are present in the joint during aging then c_{eq} increases faster than c.

This was implemented by undertaking a fully coupled stress-diffusion analysis in which c_{eq} was obtained by using a USFLD routine in which S was calculated at each integration point using the following recursion algorithm:

$$S_{t+\Delta t} = S_t + \Delta t \times \frac{dS}{dt}.$$

The enhanced degradation parameters were then transferred to a subsequent failure analysis. In the failure analysis, the CZM parameters were set to be a function of the c_{eq} instead of c.

Various analyses were undertaken to determine A and the threshold stress σ_t by correlating the numerical results with the modelling. The best-fit parameters can be seen in Table 4.

The results can be seen in Fig. 10. There was a good correlation between the numerical simulation and the experimental results for all aging times except the joint aged for 52 weeks, where the strength apparently increased. This increase in strength is not yet fully understood, but the failure mode was not significantly different from that at 26 weeks, and control specimens showed no postcure over this period.

TABLE 4 Parameters Determined for the Stress-Enhanced Degradation

A (s^{-1} MPa^{-1})	σ_t (MPa)
1.3×10^{-6}	4

3.3. Predicting the Response of the Aluminium L-Joint

The L-joint was modelled in only 3D because the overlap was 25×25 mm, so moisture diffusion in all directions was equally significant. Various analyses were carried out for the dry joint with different mesh sizes because the 3D model was computationally expensive and using a coarser mesh reduced the computational time considerably. The mesh sizes considered were $0.125 \times 0.35 \times 0.95$ mm, $0.06 \times 0.2 \times 0.5$ m, and $0.06 \times 0.15 \times 0.4$ mm. The mesh with the intermediate mesh size can be seen in Fig. 21. Both the substrates and the adhesive were modelled with eight-noded brick elements.

The predicted response of the dry L-joint using the CZM parameters determined with different mesh sizes can be seen in Fig. 22. The analyses with different mesh sizes gave very similar results. This indicated that the mesh size was small enough to ensure that the PZL was continuous for all three meshes. Thus, the coarsest mesh was used in the subsequent analysis of the wet joints.

The predicted load-displacement curve is compared with the experimental results in Fig. 22 for the dry joint. The predicted strength was marginally underestimated. Both the experimental data and numerical simulation showed the same type of failure: first progressive and then, at the end, catastrophic (Fig. 22). The initial mismatch in joint stiffness is due to machine displacement, which was present in the experiment but was not included in the FE modelling.

The simulated crack growth through the dry L-joint was as expected because it was under plane-strain-type conditions in the centre of the joint and plane stress at the edge. The simulated crack growth correlated well with the image of the failure surface (Fig. 23), with the crack propagation in the centre in advance of that of the edges. Both simulated and actual crack fronts were curved, with crack growth being more advanced in the centre than at the edge.

The crack propagation through the dry joint can be seen in Fig. 24a and 24c (showing the displacement and load at which the CZM released at each point in the adhesive). As seen in Fig. 24a, the crack propagates slightly faster in the centre of the joint. The corresponding propagation in a joint aged for 52 weeks can be seen in Figure 24b

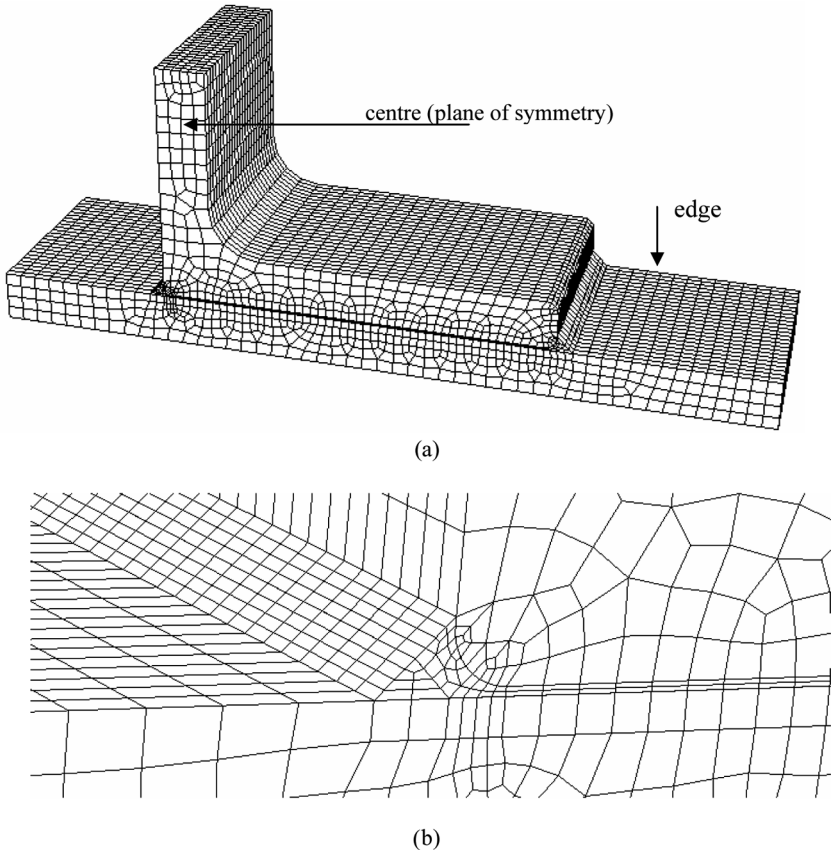

FIGURE 21 a) Intermediate mesh used for the L-joint and b) close-up of the heel.

and 24d. The crack propagated with an increase in load through wet adhesive until the dry adhesive was reached (Fig. 24d). In the exposed joints, the crack propagated faster at the wet edge than in the centre of the joint (Fig. 24b).

3.3.1. Cathodic Delamination

The predicted strength of the L-joints can be seen in Fig. 11. The rate of degradation for the predicted joints was slower than that found experimentally. There were signs of corrosion on the substrates and debonding of the adhesive before testing on some of the joints. This might be due to an electrochemical process (because the joints were immersed in tap water and not deionised water) in the form of cathodic

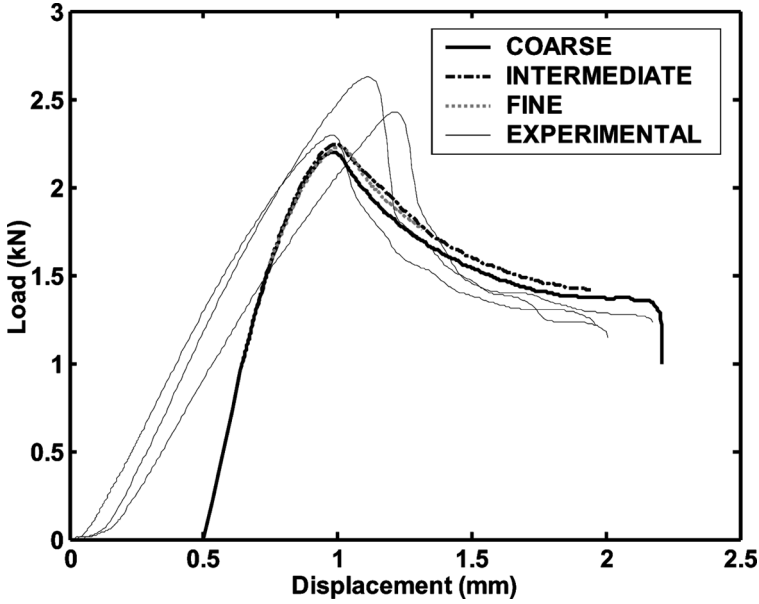

FIGURE 22 Predicted (three different mesh sizes) and experimental load-displacement responses of the L-joint.

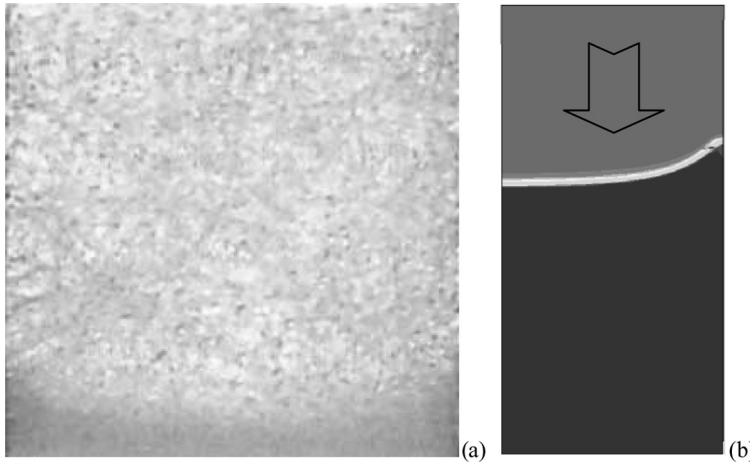

FIGURE 23 Comparison between the experimental crack propagation and the modelled crack propagation in the dry joint: a) image of L-joint surface and b) the modelled damage in the dry joint (light and dark gray represent failed and undamaged elements, respectively).

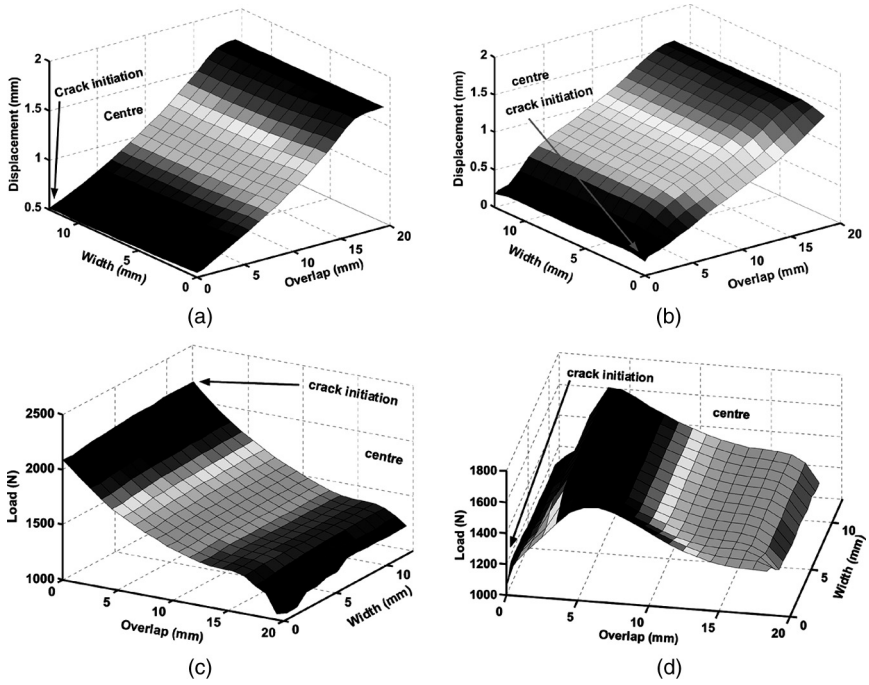

FIGURE 24 Load and displacement at crack propagation (CZM element failure) through the L-joint (3D, coarse mesh): a) displacement (dry), b) displacement (wet, 365 days immersion), c) Load (dry) and d) load (wet, 365 days immersion).

delamination [11]. Cathodic delamination consists of the following reactions (Fig. 25): electrons of the free exposed aluminium surface are dissolved

$$Al \rightarrow Al^{3+} + 3e^{-}$$

and in the relatively anodic region covered with epoxy, oxygen and water react with the electrons to produce hydroxyl ions:

$$O_2 + 2H_2O + 4e^{-} \rightarrow 4OH^{-}.$$

Hydroxyl ions are deleterious [38] to the interface strength, the adhesive debonds, the newly exposed aluminium now acts as cathode, and the remaining bonded overlap acts as the anode. This process continues until the whole overlap has debonded.

Cathodic delamination in the L-joints was modelled as follows. Delamination was set to occur when the adhesive had experienced a

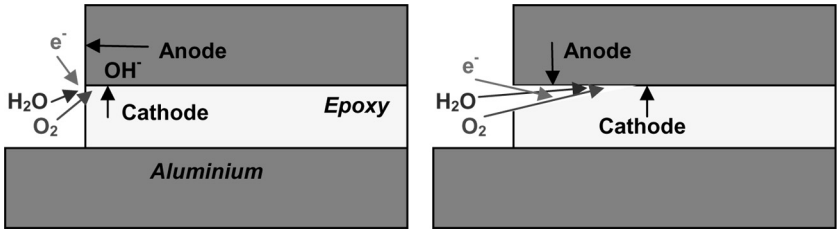

FIGURE 25 Schematic representation of cathodic delamination in an adhesively bonded joint.

critical moisture content for a certain period of time. After delamination had occurred, the diffusion was set to be very fast at the critical location in question, thus moving the boundary conditions forward. The parameters are the *critical moisture content* above which delamination occurs and the time for delamination to occur after this level has been achieved (*delay time*). This was implemented using the USFLD routine in a diffusion analysis.

The delamination parameters (moisture concentration and delamination flag) were then transferred to a failure analysis. In the failure analysis, the CZM strength was set to zero at material points where delamination was flagged as having occurred. Elsewhere the CZM strength was dependent on the moisture concentration.

The effect of using different parameters is seen in Fig. 10. The critical moisture content governs when the delamination occurs, whereas the delay time determines the rate once the delamination has started. A critical moisture content of 0.99% of the saturation level in combination with a delay time of 2 weeks was seen to give a reasonable prediction.

4. CONCLUSIONS AND FUTURE WORK

The ingress of moisture in the adhesives was determined with gravimetric experiments. The uptake rate was seen to be strongly dependent on the temperature but essentially unaffected by the moisture saturation level. The saturation level increases, as expected, with the RH for all bulk specimens.

The fracture energy for various moisture concentrations was determined with MMF and NCA specimens. The fracture energy was seen to decrease significantly in the presence of water at the interface.

The CZM parameters were determined from these tests. The tripping traction could be determined from the load-displacement

response of the MMF joint by identifying the onset of nonlinearity. When the tripping traction had been determined in this way, the fracture energy (Γ_0) was determined by correlating the experimental failure load to the simulated failure load. The CZM for immersion in water was determined from the experimental NCA specimen test results.

The determined parameters have been used to predict the residual strengths of a number of different joint configurations. The predictions of the aluminium SLJ aged by immersion in deionised water were good. For the aluminium joints that were stressed during aging, stress-enhanced degradation had to be included. The model parameters were determined by correlation of the experimental failure load with the results from the simulations. Stress-enhanced diffusion did not contribute significantly to the rate of degradation.

The prediction of the dry L-joint was good. However, the wet predictions were overestimated. Therefore, cathodic delamination was included in the model because the joints were immersed in tap water. When including this degradation mechanism, the experimentally determined reduction could be simulated.

Despite the developments, the effect of corrosion and stress has to be studied in greater detail and the models improved further.

ACKNOWLEDGEMENT

The authors gratefully acknowledge the Ministry of Defence for funding and QinetiQ for manufacturing and testing of the SLJ and the L-joints.

REFERENCES

[1] Gledhill, R. A., Kinloch, A. J., and Shaw, S. J., *J. Adhes.* **11**, 3–15 (1980).
[2] Armstrong, K. B., *Int. J. Adhes. Adhes.* **17**, 89–105 (1997).
[3] Wylde, J. W. and Spelt, J. K., *Int. J. Adhes. Adhes.* **18**, 237–246 (1998).
[4] Verhoff, J., Ramani, K., Blank, N., and Rosenberg, S., *J. Adhes. Sci. Technol.* **16**, 373–393 (2002).
[5] Neumann, S. and Marom, G., *J. Mater. Sci.* **21**, 26–30 (1986).
[6] Petropoulus, J. H. and Sanopoulou, M., *J. Polym. Sci. B* 1087–1099 (1988).
[7] Roy, S., Vengadassalam, K., Wang, Y., Park, S., and Liechti, K. M., *Int. J. Solids Struct.* **43**, 27–52 (2006).
[8] Gledhill, R. A. and Kinloch, A. J., *J. Adhes.* **6**, 315–330 (1974).
[9] Korenburg, C. F., Kinloch, A. J., and Watts, J. F., *J. Adhes.* **80**, 169–201 (2004).
[10] Linossier, I., Gaillard, F., Romand, M., and Nguyen, T., *J. Adhes.* **70**, 221–239 (1999).
[11] Davis, S. J. and Watts, J. F., *J. Mater. Chem.* **6**, 479–493 (1996).
[12] Kinloch, A. J., Korenberg, C. F., Tan, K. T., and Watts, J. F., *The Durability of Structural Adhesive Joints*, *7th EURADH 2004*, (Freiburg, Germany, 2004).

[13] Deflorian, F. and Rossi, S., *J. Adhes. Sci. Technol.* **17**, 291–306 (2003).
[14] Sargent, J. P., *Int. J. Adhes. Adhes.* **25**, 247–256 (2005).
[15] Comyn, J., *Durability of Structural Adhesives* (Applied Science Publishers, London, 1983), Chap. 3, pp. 85–139.
[16] Lam, D. C., Yang, F., and Tong, P., *IEEE T. Compon. Pack. T.* **22**, 215–220 (1999).
[17] Adams, R. D. and Peppiat, N. A., *J. Strain Anal.* **9**, 185–196 (1974).
[18] Adams, R. D., Atkins, R. W., Harris, J. A., and Kinloch, A. J., *J. Adhes. Adhes.* **20**, 29–33 (1986).
[19] Adams, R. D. and Harris, J. A., *Int. J. Adhes. Adhes.* **7**, 69–80 (1987).
[20] Crocombe, A. D. and Adams, R. D., *J. Adhes.* **13**, 241–267 (1982).
[21] Crocombe, A. D., *Int. J. Adhes. Adhes.* **9**, 145–153 (1989).
[22] Akisanya, A. R. and Meng, C. S., *J. Mech. Phys. Solids* **51**, 27–46 (2003).
[23] Wahab, M. A., *J. Adhes. Sci. Technol.* **14**, 851–865 (2000).
[24] Shirani, A. and Liechti, K. M., *Int. J. Fracture* **93**, 281–314 (1998).
[25] Rahul-Kumar, P., Jagota, A., Bennison, S. J., Saigal, S., and Muralidhar, S., *Acta Mater.* **47**, 4169–4169 (1999).
[26] Yang, Q. D., Thouless, M. D., and Ward, S. M., *Int. J. Solids Struct.* **38**, 3251–3262 (2001).
[27] Madhusudhana, K. S. and Narasimhan, R., *Eng. Fracture Mech.* **69**, 865–883 (2002).
[28] Crocombe, A. D., Hua, Y. X., Loh, W. K., Wahab, M. A., and Ashcroft, I. A., *Int. J. Adhes. Adhes.* **26**, 325–336 (2006).
[29] Liljedahl, C. D. M., Crocombe, A. D., Wahab, M. A., and Ashcroft, I. A., *J. Adhes. Sci. Technol.* **19**, 525–547 (2005).
[30] Loh, W. K., Crocombe, A. D., Abdel Wahab, M. M., and Ashcroft, I. A., *Int. J. Adhes. Adhes.* **25**, 1–12 (2005).
[31] Albrecht, P. and Mecklenburg, M. F., *The First International Conference in Composites in Infrastructure* (Tucson, Arizona, 1996), pp. 152–165.
[32] Liljedahl, C. D. M., Crocombe, A. D., Wahab, M. A., and Ashcroft, I. A., *Int. J. Adhes. Adhes.* (in press).
[33] Wang, C. H. and Chalkley, P., *Int. J. Adhes. Adhes.* **20**, 155–164 (2000).
[34] Liljedahl, C. D. M., Crocombe, A. D., Wahab, M. A., and Ashcroft, I. A., *Int. J. Fracture* (in press).
[35] Doolittle, A. K., *J. Appl. Phys.* **22**, 1471–1475 (1951).
[36] Neumann, S. and Marom, G., *J. Compos. Mater.* **21**, 68–80 (1987).
[37] Fahmy, A. A. and Hurt, J. C., *Polym. Compos.* **1**, 77–80 (1980).
[38] Watts, J. F. and Castle, J. E., *J. Mater. Sci.* **19**, 2259–2272 (1984).